https://doi.org/10.1016/j.corsci.2022.110153

Oxidation behavior of the $Ti_{38}V_{15}Nb_{23}Hf_{24}$ refractory high-entropy alloy at elevated temperatures

Di Ouyang [a, b], Zheng-jie Chen [c], Hai-bin Yu [c], K. C. Chan [b], Lin Liu [a, *]

a State Key Laboratory of Material Processing and Die & Mould Technology and School of Materials Science and Engineering, Huazhong University of Science and Technology, Wuhan, 430074, China

b Department of Industrial and Systems Engineering, The Hong Kong Polytechnic University, Hung Hom, Kowloon, Hong Kong, 999077, China

c Wuhan National High Magnetic Field Center and School of Physics, Huazhong University of Science and Technology, Wuhan, 430074, China

Abstract

The oxidation behavior of the $Ti_{38}V_{15}Nb_{23}Hf_{24}$ refractory high-entropy alloy (RHEA) in air was systematically studied in this work. Two distinct types of oxidation behavior were observed. Below 1000°C, a dense composite oxide scale with highly consistent lattice constant and crystallographic orientation was formed on the surface, while above 1000°C, internal oxidation with the formation of needle-like HfO_2 occurred in the alloy matrix below the alloy-scale interface. The internal oxidation is caused by the sufficient inward-diffusing oxygen after the decomposition of dense outer oxide layer with sluggish oxygen diffusivity. This research provides new understanding for the development of new antioxidation RHEAs.

***Keywords**:* Refractory high-entropy alloy; High-temperature corrosion; Internal oxidation

---

[*] Corresponding author: lliu2000@mail.hust.edu.cn (Lin Liu)

1. Introduction

High-entropy alloy (HEAs) are novel multicomponent alloys widely developed in the recent past [1]. In contrast to the classical alloy design approach, HEAs do not have a certain base element but consist of multiple principle elements in nearly equimolar ratios [2]. HEAs exhibit high mixing entropy, serious lattice distortion, sluggish element diffusion, etc. which enable HEAs unique properties such as high strength and ductility at cryogenic temperatures, high specific strength at elevated temperatures, excellent fracture and impact toughness, and outstanding thermal stability [3, 4].

Recently, HEAs based on refractory elements (W, Mo, Ta, Nb, W, V, Hf, Cr, etc.) have been developed, and are called refractory high-entropy alloys (RHEAs) [5]. RHEAs exhibit high melting points, strength retention and thermal stability at elevated temperatures. Thus, they are considered as novel materials to serve in high temperature environments and are potential to replace the commonly used nickel-based superalloys [6-8].The first two RHEAs, MoNbTaW and MoNbTaVW, were reported in 2010 by Senkov et al. [9]. They found that the two alloys were single-phase body-centered cubic (BCC) structure which retained high yield strength (above 400 MPa) at temperatures even up to 1600°C [10]. Later on, more alloy systems such as ZrNbAlTiV [11], ZrNbMoTaW [12], MoNbTaTiVW [13], TiVNbMoZr [14] etc. were explored. Unfortunately, these alloys all exhibited extreme brittleness at ambient temperature. Among about 150+ HEAs developed so far, only a very few alloy systems, including HfNbTaTiZr [15], NbTiVZr [16], TiZrHfNb [17], TiVNbHf [18] have been shown to have sufficient plasticity at room temperature.

It is well know that the poor high-temperature oxidation resistance is a primary limitation for the widespread implementation of refractory elements and their alloys, and RHEAs similarly encounter the same problems [19]. Refractory elements tend to form a loose oxide scale or volatile oxides in air when temperature is rising, making oxygen diffuse into the alloy matrix continuously. It has been reported that the formation of oxide in the matrix significantly reduces the strength, toughness and creep resistance of RHEAs [5]. To improve the oxidation resistance of RHEAs, Al, Cr, Si were added to form protective scales such as Al_2O_3, Cr_2O_3, and SiO_2. That is because among steady state oxides, only Al_2O_3, Cr_2O_3, SiO_2

scales are commonly accepted as sufficiently dense, thus effectively enabling the inhibition of oxygen internal diffusion and metallic ion external diffusion [20-23]. However, Al, Cr and Si are chemically active with large negative heats of mixing with other metallic elements, and therefore tend to promote the formation of undesirable brittle phases such as Sigma and Laves phases as well as aluminides and silicides, leading to the reduction of toughness and ductility [24]. In addition, for alloys containing Zr or Hf, the additions of Al, Cr and Si have a limited effect. That is because the formation of ZrO_2 and HfO_2 are more thermodynamically favorable as compared to Al_2O_3, Cr_2O_3, and SiO_2. Thus, dense protective Al_2O_3, Cr_2O_3, SiO_2 scales are almost impossible to be achieved in Zr/Hf-contained HEAs [5]. The anti-oxidation performances of the Zr/Hf- contained alloys are mainly dependent on the nature of their own oxide layers, such as the diffusion of oxygen in the oxide, the adhesion of oxide layer on the alloy matrix, etc. [25]. Wei et al. [18] compared the oxidation behavior of $Ti_{38}V_{15}Nb_{23}Hf_{24}$ and $Ti_{25}V_{25}Nb_{25}Hf_{25}$ RHEAs under 600°C, 800°C, and 1000°C, and verified that drastic catastrophic oxidation occurs in the $Ti_{25}V_{25}Nb_{25}Hf_{25}$ RHEA due to the site-preferential oxidation of Ti and Nb occurring at grain boundaries. While for the $Ti_{38}V_{15}Nb_{23}Hf_{24}$ RHEA, comparatively more decent oxide scale forms on the surface, and no evident of pest oxidation or spallation is detected, leading to a lower oxidation rate. Sheikh et al. [24] revealed that the pesting mechanism in a $Hf_{0.5}Nb_{0.5}Ta_{0.5}Ti_{1.5}Zr$ RHEA is attributed to the failure in forming protective oxide scales accompanied by the accelerated internal oxidation. The simultaneous removal of Hf, Zr can eliminate the pesting phenomenon in the alloy. Pole et. al [26] investigated the tribological behavior of HfTaTiVZr and TaTiVWZr RHEAs at elevated temperatures. They found that the wear rates of them is initially increased up to the temperature of 423 K, then decreased with further increasing temperature, which is due to a transition from abrasive to oxidative wear mechanism with the formation of stable oxides and its subsurface deformation in the contact region. The nature of the oxide behaviors, such as microstructure, phase formation, lattice defects are constantly changed at elevated temperatures [27], which radically alters the oxidation process of RHEAs. Therefore, it is important to understand the features of the oxide layer and the corresponding effects on the oxidation behaviors. However, such issues are still lack in literatures for Zr/Hf- contained

RHEAs.

In this work, we chose a Hf-contained RHEA of $Ti_{38}V_{15}Nb_{23}Hf_{24}$ to study the evolution of its oxides as well as oxidation behavior in air at elevated temperatures. Interestingly, it is found that the oxidation behavior of the RHEA is closely related to the reaction temperature. When the temperature is lower than 1000°C, the RHEA is oxidized with a layer of dense composite oxide, having a highly consistent lattice constant and crystallographic orientation on its surface. In contrast, above 1000°C, the internal oxidation of the growth of needle-like HfO_2 occurs in the alloy matrix below the alloy–scale interface. The decomposition of the dense outer oxide layer above 1000°C is identified as the causation of internal oxidation, as the nucleation and growth of needle-like HfO_2 in the matrix need sufficient inward-diffusing oxygen. This research on the oxidation behavior of Hf-contained RHEA under various temperatures provides new cognition for the development and design of new antioxidation RHEAs.

2. Materials and Methods

The primary alloy of $Ti_{38}V_{15}Nb_{23}Hf_{24}$ (at.%) was prepared using high purity (> 99.9%) elemental metals by magnetic levitation melting in an Ar atmosphere. Cuboids with dimensions of 6 mm × 10 mm × 65 mm were finally fabricated by suction casting in a copper mold. Specimens with dimensions of 1.5 mm × 3 mm × 5 mm were extracted from the cuboids by wire-cutting for the oxidation tests. Differential thermal analysis (DTA, TA STD 600) was used to study the oxidation kinetics of RHEAs and pure metals in air. X-ray diffraction (XRD, Bruker D2 phaser) with Cu Kα radiation was used to detect the phase features of alloy and oxides. The oxide scale was successively removed by mechanically grinding (2000# abrasive paper) about 10 μm thickness per layer and tested the XRD device, until the interior alloy substrate appeared. The grain size of RHEAs was examined by optical microscopy (OM, Leica DFC450) after being polished and etched with a corrosive agent (mixture of 1.5 ml HF, 3 ml HNO_3, 3.5 ml HCl and 6 ml H_2O). The microstructure of the oxide scales was characterized by scanning electron microscopy (SEM, Nova Nano SEM 450) under a back scattered electron (BSE) model. The detailed microstructure of the oxides, the boundary between oxide and alloy matrix was further examined by transmission electron microscopy (TEM, FEI Tecnai G20). TEM thin foils were prepared using a focused ion beam (FIB, Quanta 3D FEG). In order to reveal the preferential growth of HfO_2 in the alloy matrix, MD simulation with a canonical ensemble (NVT) was implemented by density functional theory (DFT) using the Vienna ab initio simulation package (VASP). The detailed calculation methods are reported in the literature [28].

3. Results

The XRD pattern of $Ti_{38}V_{15}Nb_{23}Hf_{24}$ RHEA prepared by suction casting is shown in **Fig. 1a**, similar to the previous work [18], the HEA exhibits a single-phase BCC structure without any other precipitated phases. **Fig. 1b** shows the OM image of the as-cast RHEA, in which the grains are equiaxial with average grain size of 53 μm calculated by ImageJ software. To detect the oxidation behavior of the RHEA under various temperatures, we respectively chose a range of temperatures (700, 800, 900, 1000, 1100, 1200 and 1300℃) to perform the isothermal oxidation tests (60 mins in air) by DTA (**Fig. 2**). When for isothermal temperatures of 700℃, 800℃ and 900℃, the oxide scales on the surface of the alloy matrix are homogeneous and dense, a characteristic of external oxidation behavior. In contrast, the morphologies of the oxide scales are completely different for isothermal temperatures of 1000℃ ~ 1300℃. White precipitated particles as well as pores occurred in the oxide scales, and the porosity of the oxide scales increased with the elevated temperatures. Besides, a large amount of vimineous needles occurred in the alloy matrix below the alloy–scale interface, exhibiting an internal oxidation [29]. Therefore, the oxidation mechanism changes around 1000℃, from an external oxidation process to an internal oxidation process. Based on the oxide layer thickness, it can be seen that the transition from external to internal oxidation significantly accelerates the oxidation process of RHEA. The curves of the mass gain of the studied RHEAs during the oxidation process at various temperatures are displayed in **Fig. 2h**. At temperatures of 700℃ to 900℃, the slopes of the mass gain curves gradually increase with enhanced temperatures, which means that the oxidation process is accelerated with increasing temperature. However, the slope of the mass gain curve is suddenly reduced at 1000℃ and even smaller than 900°C. By comparing the thickness of the oxide layers at 1000°C and 900°C, we found that the depressed slope at 1000°C isn't caused by the enhanced anti-oxidation performance, but the evaporation of V_2O_5 among the oxides, as there is no other volatile matter involved [19]. Above 1000°C, the slopes of the mass gain curves are also gradually increased with enhanced temperature. The results demonstrate that 1000°C is the critical temperature for occurrence of the transition from external oxidation to internal oxidation of the RHEA.

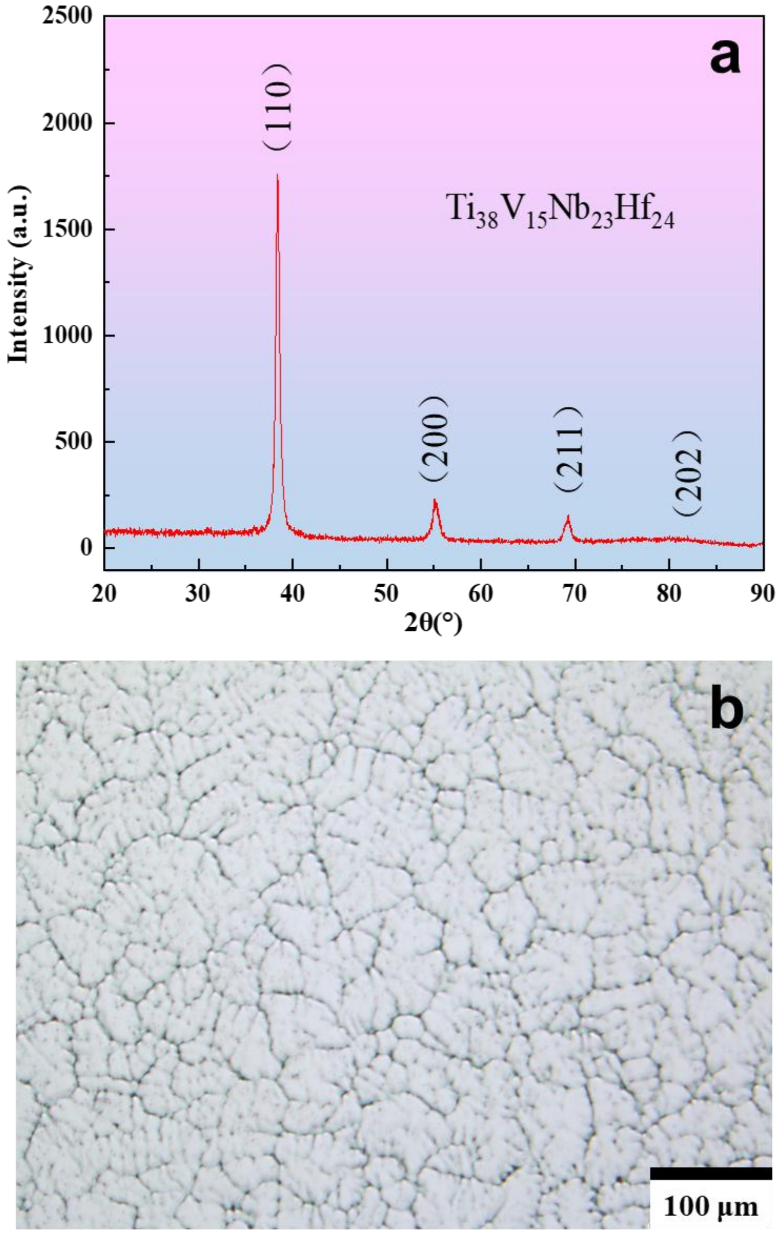

Fig. 1 Microstructural characterization of RHEA: (a) XRD; (b) OM.

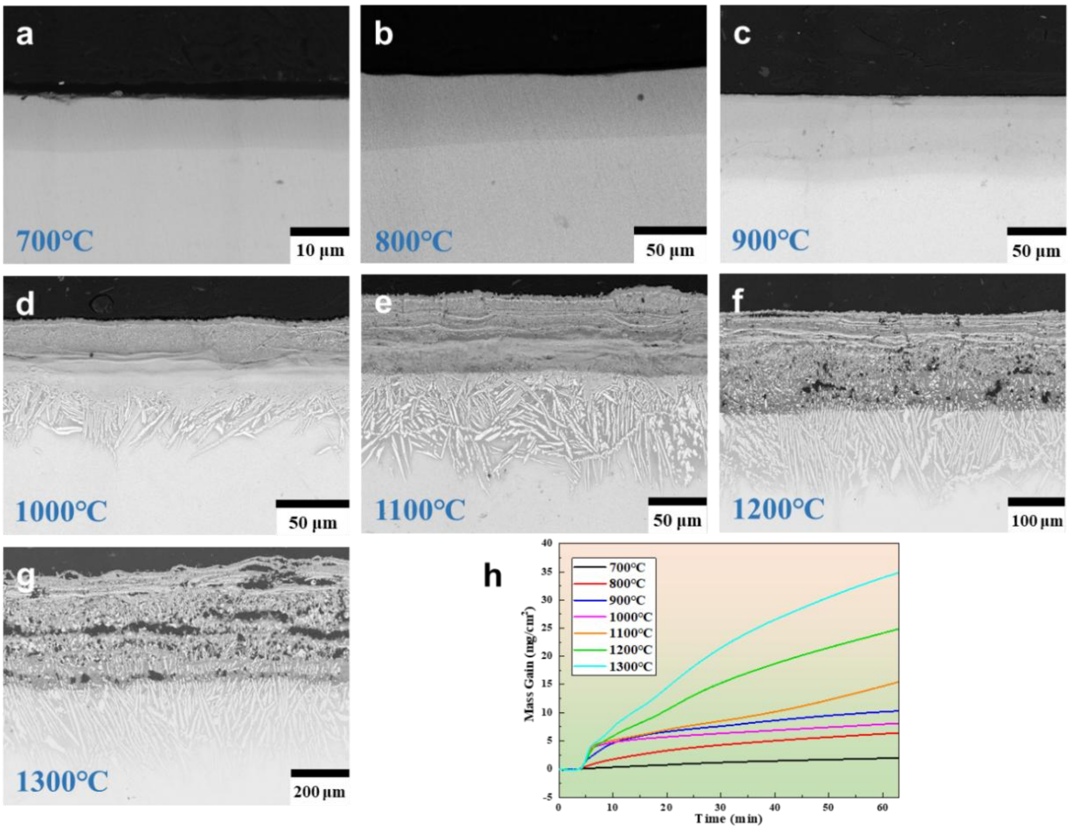

Fig. 2 (a-g) SEM-BSE images of RHEA oxide layers under various temperatures (60min in air); (h) Mass gains per unit area as a function of oxidation time for the RHEA under various temperatures in air.

To clarify the mechanism of the transition, two representative temperatures (900°C and 1000°C) were selected and further investigated. **Fig. 3** shows the XRD patterns of RHEA oxide layers at different depths at 900°C and 1000°C (for 60min in air). At 900°C, mixed oxides of $Ti_2Nb_{10}O_{29}$ and $Hf_6Nb_2O_{17}$ were observed in the topside of the oxide layer, which gradually turns to particularly dense composite oxides of $(TiVNbHf)_{100-x}O_x$ with FCC structure. The diffraction peaks of $(TiVNbHf)_{100-x}O_x$ in the XRD patterns are quite wide, indicates that its grains are ultra-fine. Meanwhile, slight $V_2Ti_7O_{17}$-like oxides coexists in the composite oxides. By comparison, the top-surface of the oxide scale of 1000°C consists of $TiNb_2O_7$ and Nb_2O_5, and below the top-surface, the fractions of $V_3Ti_6O_{17}$ and HfO_2 gradually enhance with the increasing oxide layer depth. The region of the needle layer only exhibits the XRD patterns of HfO_2 and BCC matrix, which means that the needles are all HfO_2 precipitates in the alloy matrix. Clearly, when the temperature reaches 1000°C, the growth of needle-like HfO_2 in the alloy matrix is accompanied with the variation of the phase and microstructure in the outside oxide scale.

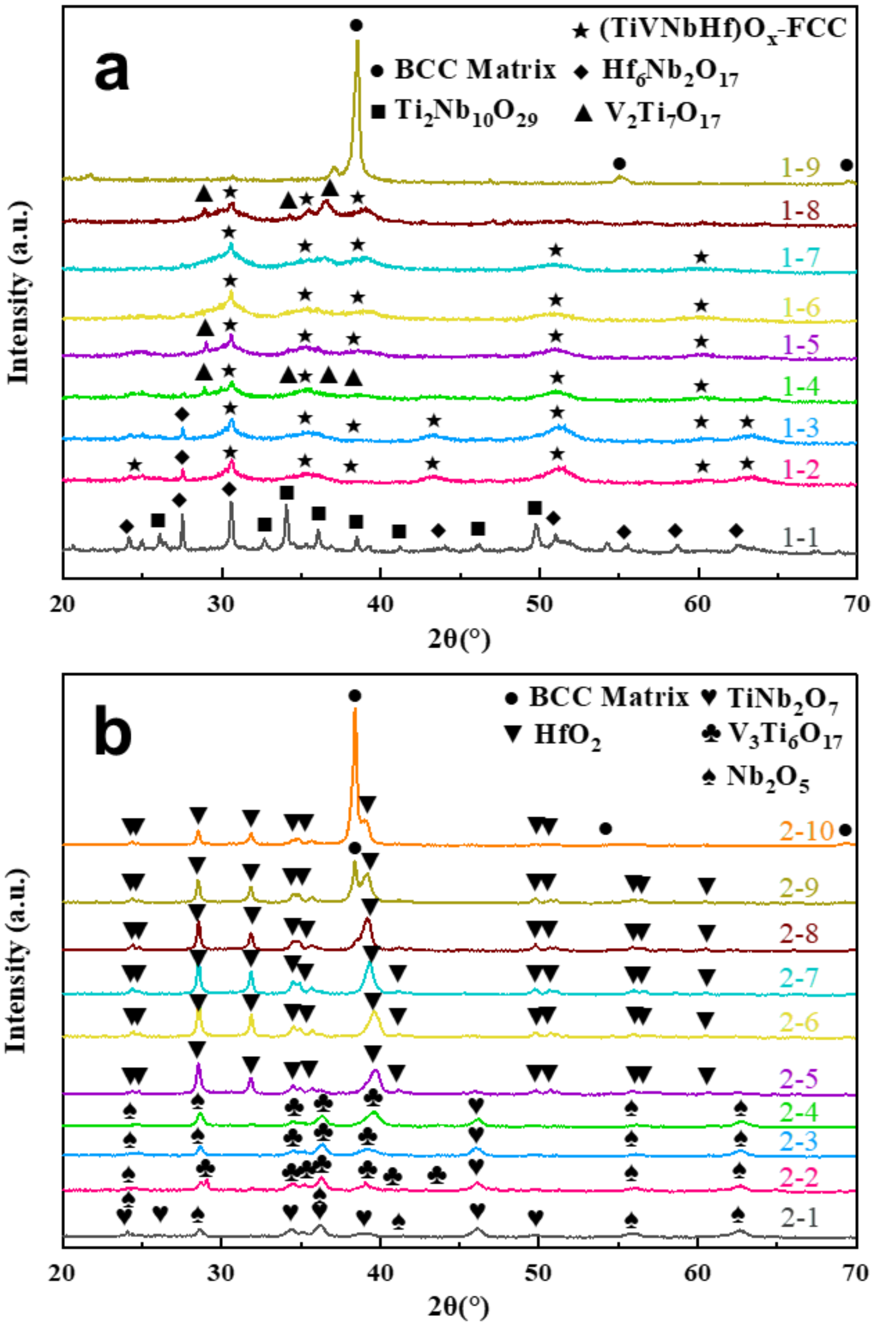

Fig. 3 XRD patterns in different depth of RHEA oxide layers: (a) 900°C-60min in air; (b) 1000°C-60min in air, the corresponding positions are shown in Fig. S1.

In order to observe the detailed microstructure of the dense oxide layer at 900°C, a small area around the position of points 1-3 in **Fig. 3a** was extracted by FIB and examined by TEM, and the results are illustrated in **Fig. 4**. The bright-field TEM image (**Fig. 4a**) indicates that the oxide layer is composed of fine nanocrystallites with grain size below 10 nm. Notably, a mass of Moire patterns (commonly caused by the parallel crystal planes with different interplanar spacing [30]) appear, which is also verified by the high resolution bright-field (HRTEM) in **Fig. 4c**. Besides, the inset image of Fourier Transform (FFT) shows that the grain orientations of nanocrystallites of $(TiVNbHf)_{100-x}O_x$ are consistent with the corresponding selected-area electron diffraction (SAED) patterns of **Fig. 4b**. Interestingly, the electron diffraction patterns exhibit a set of single-crystal electron diffraction patterns, indicating the nanocrystalline oxides formed are highly orientated. The patterns can be indexed by two main phases (Phase 1 and Phase 2) with face-centred cubic (FCC) structure and lattice constant a = 0.522 nm and 0.495 nm, respectively. These features are in consistent with the XRD results. Apart from the strongest diffraction spots, there are abundant weak diffraction spots surrounding the central transmission spot and diffraction spots, which correspond to the diffraction from the Moire patterns and possibly second diffraction patterns. This is confirmed by the Dark-field TEM image shown in **Fig. S2**. The STEM-HAADF image and corresponding elemental mapping are presented in **Fig. 4d-j.** It is clear that all the metallic elements appear minor segregation, to some extent, despite the uniformly distributed oxygen. Further, the Ti, V, Nb tend to gather together and the Hf tends to stay separately, leading to the existence of Hf-enriched regions and Hf-poor regions. These two regions correspond to the two phases as illustrated in **Fig. 4b**. The minor segregation of the elements causes the lattice constants of oxides there to vary within a certain range, but the oxides retain almost the same crystal structure.

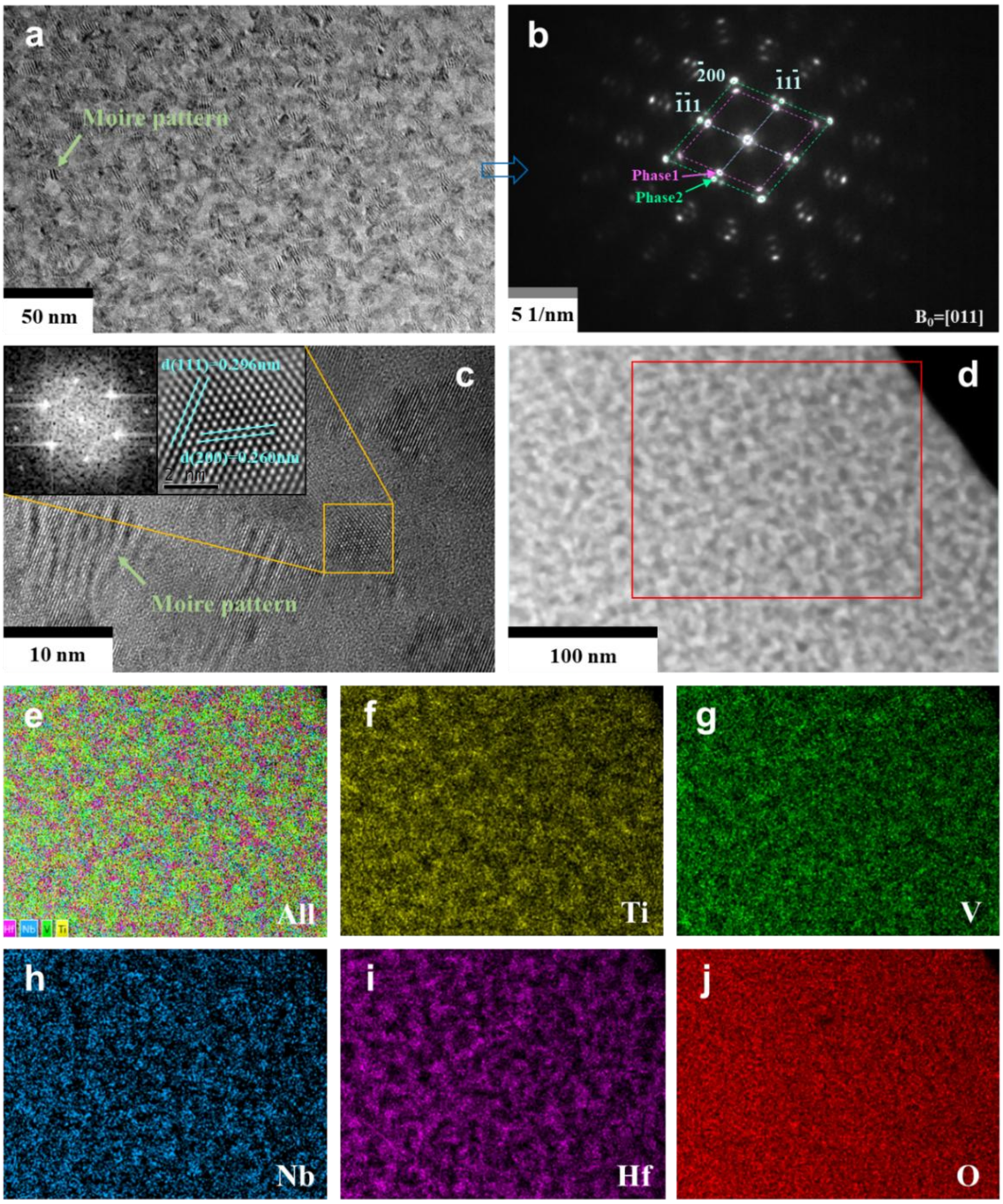

Fig. 4 TEM images of RHEA oxide layer under the condition of 900°C-60min in air: (a) Bright-field TEM image for the oxidation layer, (b) The corresponding selected-area electron diffraction (SAED) patterns of (a); (c) High resolution bright-field (HRTEM) morphology from (a); (d) The High angle annular dark field (STEM-HAADF) image of RHEA oxidation layer; (e-j) The corresponding elemental distribution for the selected area of (d).

The detailed microstructure of the oxide scale at 1000°C was also examined by SEM, as illustrated in **Fig. 5**. In which, the oxide scale presents a hierarchical structure. The outermost layer (~5 μm) is composed of coarse grains, which is enriched in Ti, Nb and depleted in V, Hf (see the EDX of point S1 in Table 1). Meanwhile, a mass of fine white particles precipitates in a large area below the outermost surface, accompanied by some voids. The fine white particles are oxides enriched in Hf (see the chemical composition of S2 in **Table 1**). Furthermore, in the region of internal oxidation (**Fig. 5b**), some irregular voids with size below 1 μm surround the needle-like HfO_2, and may be caused by the volumetric change due to the formation of HfO_2 needles. In which, the rapid segregation of Hf produces a large number of vacancies in the alloy matrix, and the vacancies gather and collapse to form voids. The occurrence of voids will benefit to release the phase transformation stress of oxides, but reduce the bonding strength of oxide scale on the alloy matrix. In addition, accompanied with the growth of HfO_2 needles, the content of Hf in the alloy matrix is decreased (S3 and S4 in **Table 1**).

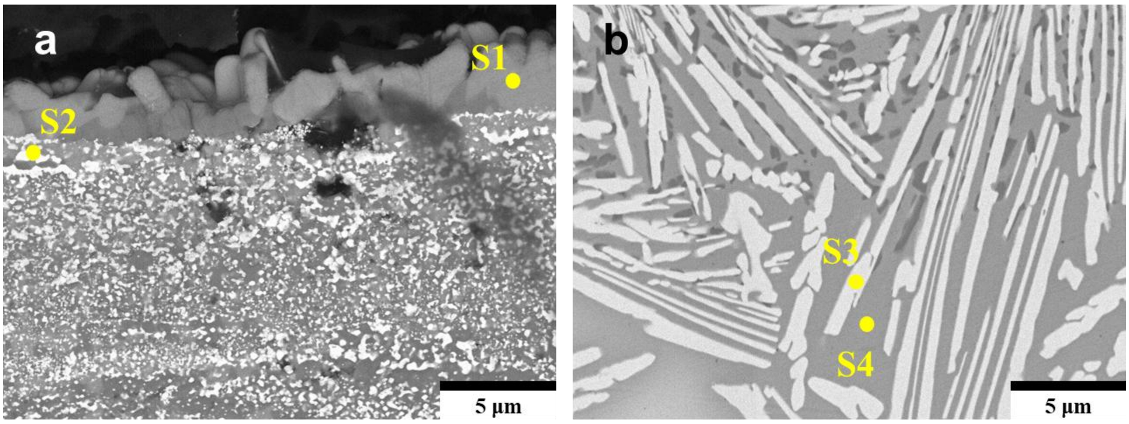

Fig. 5 SEM images of RHEA oxide layer at 1000℃ (60min in air): (a) The region of upper oxides; (b) The region of internal oxidation.

Table 1 The chemical composition in different regions in Fig. 5.

	Ti (at.%)	**V (at.%)**	**Nb (at.%)**	**Hf (at.%)**	**O (at.%)**
Nominal	38	15	23	24	0
S1	4.85 ± 1.79	1.67 ± 0.14	18.93 ± 2.10	1.88 ± 1.72	72.67 ± 5.47
S2	0.14 ± 0.07	0.21 ± 0.11	0.17 ± 0.12	29.36 ± 5.93	70.12 ± 6.23
S3	0.98 ± 0.34	0.41 ± 0.19	0.69 ± 0.20	29.14 ± 4.05	68.78 ± 4.78
S4	30.02 ± 3.43	14.82 ± 2.60	26.72 ± 2.76	3.36 ± 1.10	25.08 ± 2.49

4. Discussion

4.1 The external oxide layers of 900°C and 1000°C

The above results indicate that the dense composite oxide layer with a high consistency of oxide grain orientation is decomposed at 1000°C. Subsequently, a hierarchical structure is formed in the oxide layer. To clarify the oxidation process in air at 1000°C, we observed the features of the top oxide scale in different times (1, 5, 30, 60 min), as shown in **Fig. 6**. As the oxidation time proceeds, the outermost oxide scale gradually grows and densifies. Once a layer of dense oxide is formed, this thickness does not increase with the prolonging of the oxidation time. In other words, the formed dense oxide scale prevents the outward migration of metallic cations and produces a layer of protective scale. According to the chemical compositions (S5, S7, and S8 in **Table 2**), this dense oxide scale is enriched with Ti and Nb. Though the dense oxide scale can prevent the outward migration of metallic cations, it cannot restrain the sustaining inward migration of oxygen from the air. That's because the composite oxides of $TiNb_2O_7$ commonly contain a mass of anion vacancies, oxygen in the air can persistently be absorbed and traverses through the oxides to the alloy matrix with the help of these anion vacancies [25, 31]. For the outward migration of Ti, Nb enriched in the outermost oxide scale, element of Hf is surplus below the dense oxide scale and precipitates in the form of HfO_2 particles with a gradient distribution (**Fig. 6** and S6, S9 in **Table 2**). Thus, the HfO_2 particles in the region closer to the dense oxide scale are more luxuriant and coarsening. Besides, the HfO_2 particles also gradually grow up with the time extending, the average grain size of them are changed from 150 nm (5 min) to 500 nm (60 min) approximatively.

Table 2 The chemical composition for the selected points in Fig. 6.

	Ti (at.%)	V (at.%)	Nb (at.%)	Hf (at.%)	O (at.%)
Nominal	38	15	23	24	0
S5	5.69 ± 1.75	0.99 ± 0.08	18.77 ± 2.33	1.25 ± 0.15	73.31 ± 4.31
S6	0.96 ± 0.22	0.51 ± 0.11	0.22 ± 0.05	30.12 ± 4.76	68.19 ± 5.14
S7	7.80 ± 2.69	2.80 ± 0.86	20.71 ± 4.70	1.61 ± 0.37	67.09 ± 6.16
S8	17.01 ± 1.98	3.84 ± 1.39	7.76 ± 2.77	1.98 ± 0.64	69.41 ± 5.50
S9	0.71 ± 0.18	0.63 ± 0.21	0.48 ± 0.13	28.72 ± 4.72	69.46 ± 4.98

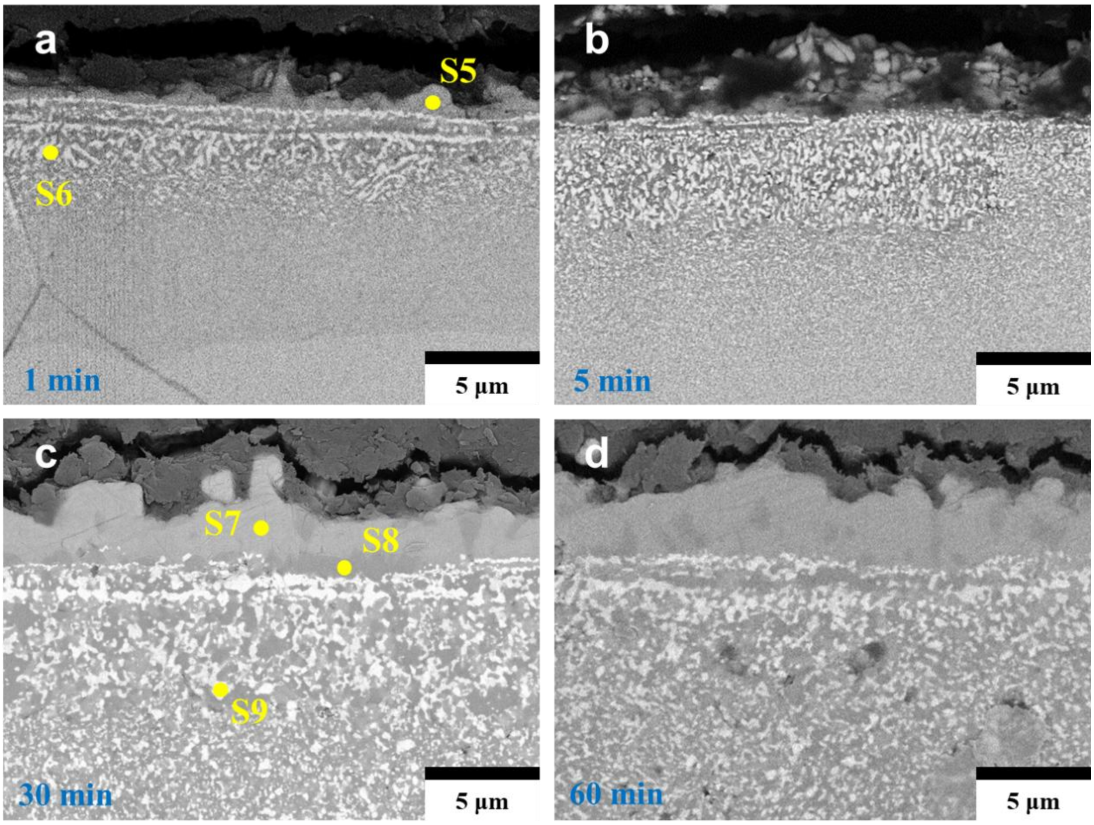

Fig. 6 High magnification SEM images of upper RHEA oxidation layers under 1000°C in air with different times: (a) 1min; (b) 5min; (c) 30min; (d) 60min.

Interestingly, HfO_2 is preferentially precipitated oxides in the oxide scales. The formation of the oxides as observed in our experiments can be rationalized by the thermodynamic aspects [27]. **Fig. 7a** shows the change of the free energy of different metal-oxides with temperature [32, 33]. It is clear that the standard free energy of HfO_2 is the most negative compared to other oxides. Besides, we also calculate the oxidation activation energy of Ti, V, Nb, Hf by Arrhenius type plot [25]. The results show that Hf (2.112 KJ/mol) possesses the lowest oxidation activation energy than others (Ti 2.759 KJ/mol, V 3.719 KJ/mol, Nb 3.431KJ/mol). Therefore, Hf shows the strongest affinity with oxygen and the precipitation of HfO_2 reduces the overall energy state to as low as possible. It is curious that the standard free energy of HfO_2 always maintains the lowest value within the range of 500-1400°C, but the precipitation of HfO_2 occurs above 1000°C. To clarify the transition from external to internal oxidation around 1000°C, the mass gain in air of the pure metals (Ti, V, Nb, Hf) and the cast

RHEA were tested by using TG under a continuous heating mode (**Fig. 7b**). Obviously, the tendency of oxidation of RHEA is consistent with the V counterpart. In the mass gain curve of V, there is a turning point before 1000°C, which is caused by the evaporation of V_2O_5, so that the weight gain of the oxidizing sample becomes sluggish [34]. We also observe some yellowish residue (corresponding to V_2O_5) in the bottom of the crucibles after heating the RHEAs to 1000°C and cooling down. This phenomenon doesn't appear in the 900°C temperature. Thus, the turning point below 1000°C in the mass gain curve of RHEA is caused by the evaporation of V_2O_5 as well. Hence, the evaporation of V_2O_5 plays an important role in the formation of the hierarchical structure in the oxide layer of RHEA above 1000°C. For that the long-range migration of metallic ions in the solid is difficult, the evaporation of V_2O_5 leaves a mass of atomic scale vacancies, which acts as a transmission channel for the outward migration of Ti, Nb ions [35], producing the outermost dense oxide scale. The precipitation and growth of the HfO_2 particles in the oxide scale can also utilize these vacancies.

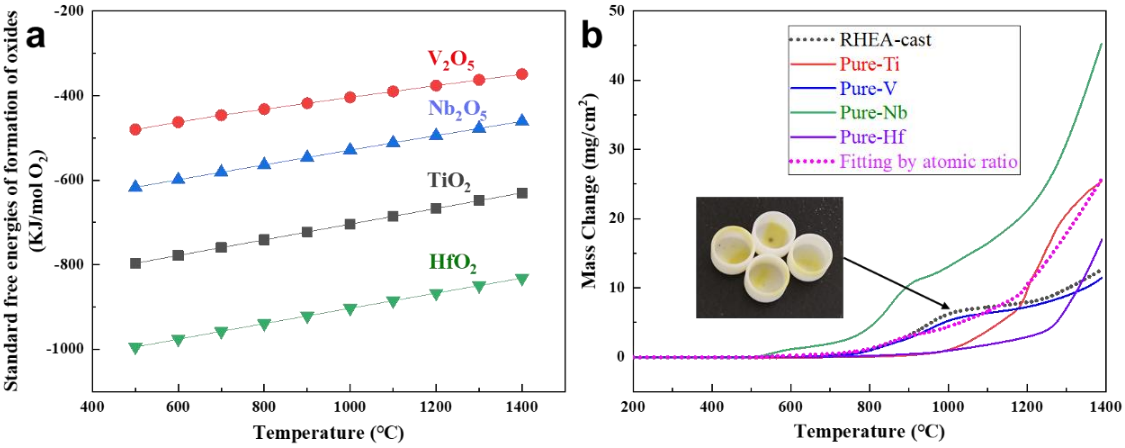

Fig. 7 (a) Standard free energies of formation of relevant oxides for RHEA; (b) The continuous mass change curves for RHEA and corresponding pure elements (10°C/min for the heating rate), the insect image shows the crucibles after heating the RHEAs to 1000°C and cooling down.

4.2 The internal oxidation above 1000 °C

Accompanied with the structural evolution in the external oxide layer above 1000°C, the needle-like HfO_2 grows inward to the alloy matrix simultaneously, namely internal oxidation. Based on the summary of Birks et al. [25], the occurrence of the internal oxidation should satisfy four essential conditions, and the sudden transition from external oxidation to internal oxidation above 1000°C in this study only comes from the sharply increased diffusivity of oxygen. That is because the other three essential conditions for internal oxidation there are immobile. Such as the value of standard free energy of formation for the precipitated metal oxide (HfO_2 in this study) must be more negative than that of the base metal oxides (oxides for Ti, V, Nb), the solute concentration (the concentration of Hf) of the alloy must be lower than that required for the transition from internal to external oxidation, and the oxygen can dissolve into the alloy. For the oxide layer at 900°C, it is dense and the nanocrystallites in it display similar lattice constant and orientation, and fewer interfaces keep the diffusivity of oxygen at a low level (**Fig. 4**), does not satisfy the condition of internal oxidation. However, the decomposition of the dense oxide layer above 1000°C produces various types of oxides with loose structures (**Fig. 5a**), which act as convenient channels for the transmission of oxygen and sharply increase the diffusivity of oxygen. Thus, the internal oxidation occurs under sufficient diffusivity of oxygen. To verify this view point, a small area around the position of FIB 2 in **Fig. S3** was extracted through FIB and examined by TEM, and the results are presented in **Fig. 8**. Apparently, the electron diffraction pattern (**Fig. 8a**) exhibits rambling polycrystalline spots, indicating various crystal types and orientations. The HRTEM images (**Fig. 8b-c)** also show a random distribution of oxide nanocrystallites with different lattice types. According to the corresponding elemental distribution of oxides in the 1000°C-sample (**Fig. 8d-j**), we find that in spite of the uniformly distributed oxygen, a larger-scale element segregation appeares. Some Nb-enriched regions occur, and Hf individually exists in some regions of the oxide layer in the form of HfO_2. While in the oxide layer of 900°C-sample, the inhomogeneously distributed elements are not completely separated and retain a consistent lattice structure of oxides. Thus, we conclude that the large-scale segregation of elements destroys the original integrated structure of composite oxides, causes the precipitation of various types of oxides and the sharply increased diffusivity of oxygen. Finally, the internal oxidation occurs in the alloy matrix under sufficient diffusivity of oxygen.

Remarkably, the internal oxidation of HfO_2 presents a needle-like morphology, which is different from the commonly observed spheres or platelets in oxide layer [36, 37]. In general, the morphology of oxide particles in oxidation is determined by a competition between the rate of nucleation as the internal oxidation front passes, and the subsequent growth rates of the oxide particles [25, 38]. The formation of elongated particles can also be promoted by inward interfacial diffusion of oxygen along the alloy oxide interfaces [39]. To observe the growth features of needle-like HfO_2 in the alloy matrix, the front of precipitated needle-like HfO_2 was further characterized by TEM after extraction by FIB at the position of FIB 3 in **Fig. S3**, with the results illustrated in **Fig. 9**. The diffraction patterns of SA2 (**Fig. 9d**) only exhibit a set of diffraction spots of HfO_2 and a set of diffraction spots of the alloy matrix, which means that the growth of needle-like HfO_2 does not induce other precipitates from the matrix and the adjacent needle-like HfO_2 retain the same orientation. Further, the precipitated HfO_2 (monoclinic structure) and alloy matrix (BCC structure) are incoherent in their interface (**Fig. 9d**). The HRTEM image in **Fig. 9b** also confirms the incoherent interface with a loose atomic arrangement, which benefits for the oxygen transferring to the growth front. The preferred growth direction the of needle-like HfO_2 is perpendicular to the $(\bar{1}01)$ plane, representing the lowest energy direction and is thermodynamically preferred. Commonly, the $(\bar{1}11)$ plane has the lowest energy state in the monoclinic HfO_2 below 400°C and exhibits the main growth face [40]. However, the energy state of the crystallographic plane changes with the temperature [28]. To clarify the preferred growth plane at 1000°C in this study, we conducted theoretical calculations using DFT (**Fig. 10a**), in which, 9 low-index crystallographic planes (present lower energy state than high-index planes) were chosen to calculate their energy changes when the HfO_2 crystal grows along them. Interestingly, the $(\bar{1}01)$ plane exhibits the largest energy decrease (**Fig. 10b**), leading to the most stable overall system during the stacking process of the Hf and O atoms. Thus, based on the elemental distribution around the front of the needle-like HfO_2 (**Fig. 9h-m**), we can speculate the growth process that once a HfO_2 nucleus is formed and grows along the crystal orientation perpendicular to the $(\bar{1}01)$ plane, Hf and O in the surrounding matrix will be consumed, causing a region nearby poor of Hf and O. The compositional gradient prompts Hf and O in distant regions gathering to the front of HfO_2, and gradually exhausts the element of Hf in the alloy matrix. Simultaneously, a few clusters of enriched Ti occur in the alloy matrix in the front of needle-like HfO_2 transitorily (**Fig. 11i**), which may be caused by the constituent fluctuations during the mass transport process of Hf.

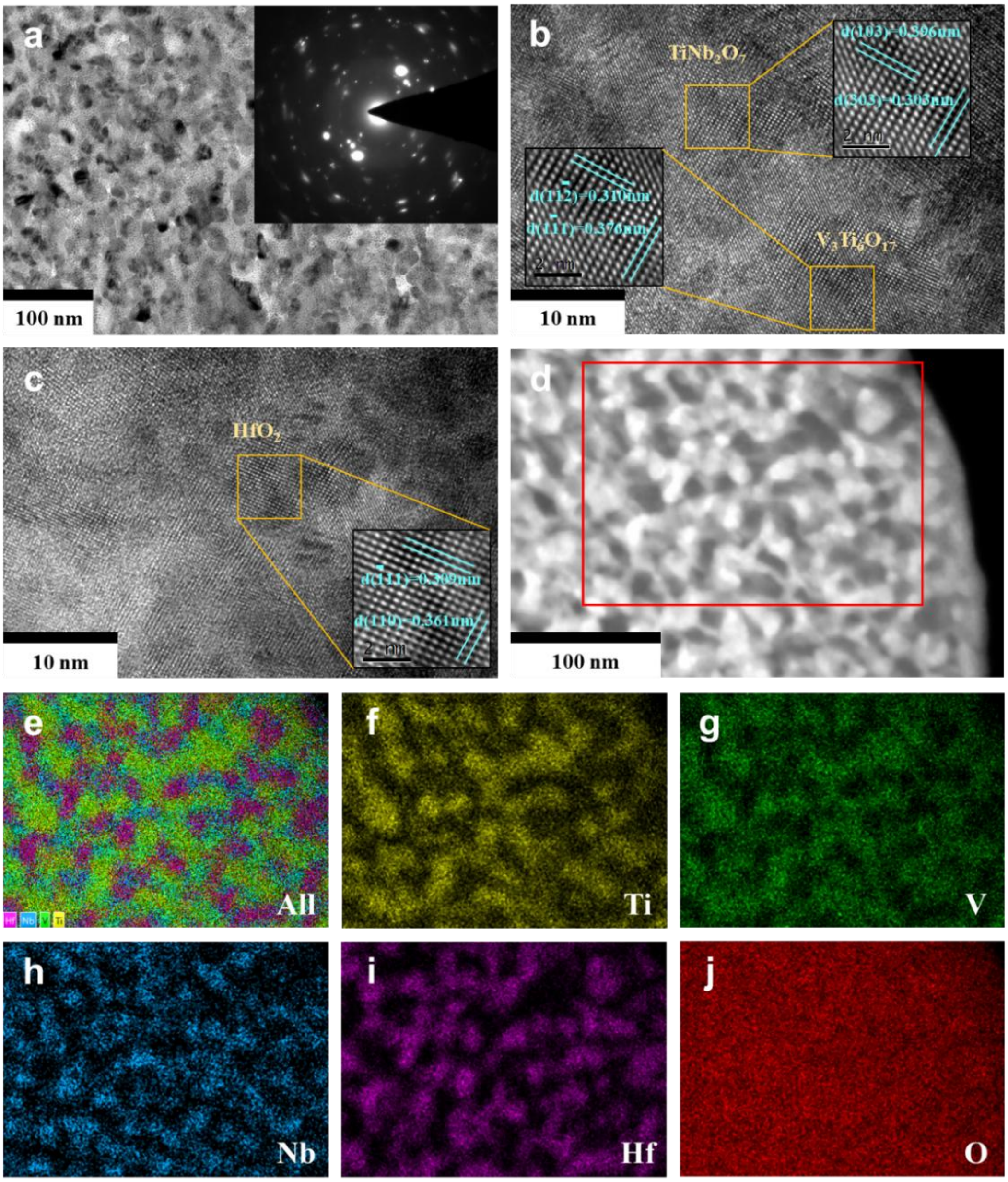

Fig. 8 TEM images of RHEA oxide layer under the condition of 1000°C-1min in air (the TEM sample was prepared by FIB as located in the position of FIB 2 in Fig. S2): (a) Bright-field TEM image, the corresponding selected-area electron diffraction (SAED) pattern is inserted; (b-c) High resolution bright-field (HRTEM) morphology from (a); (d) The STEM-HAADF image of RHEA oxidation layer; (e-j) The corresponding elemental distribution for the selected area of (d).

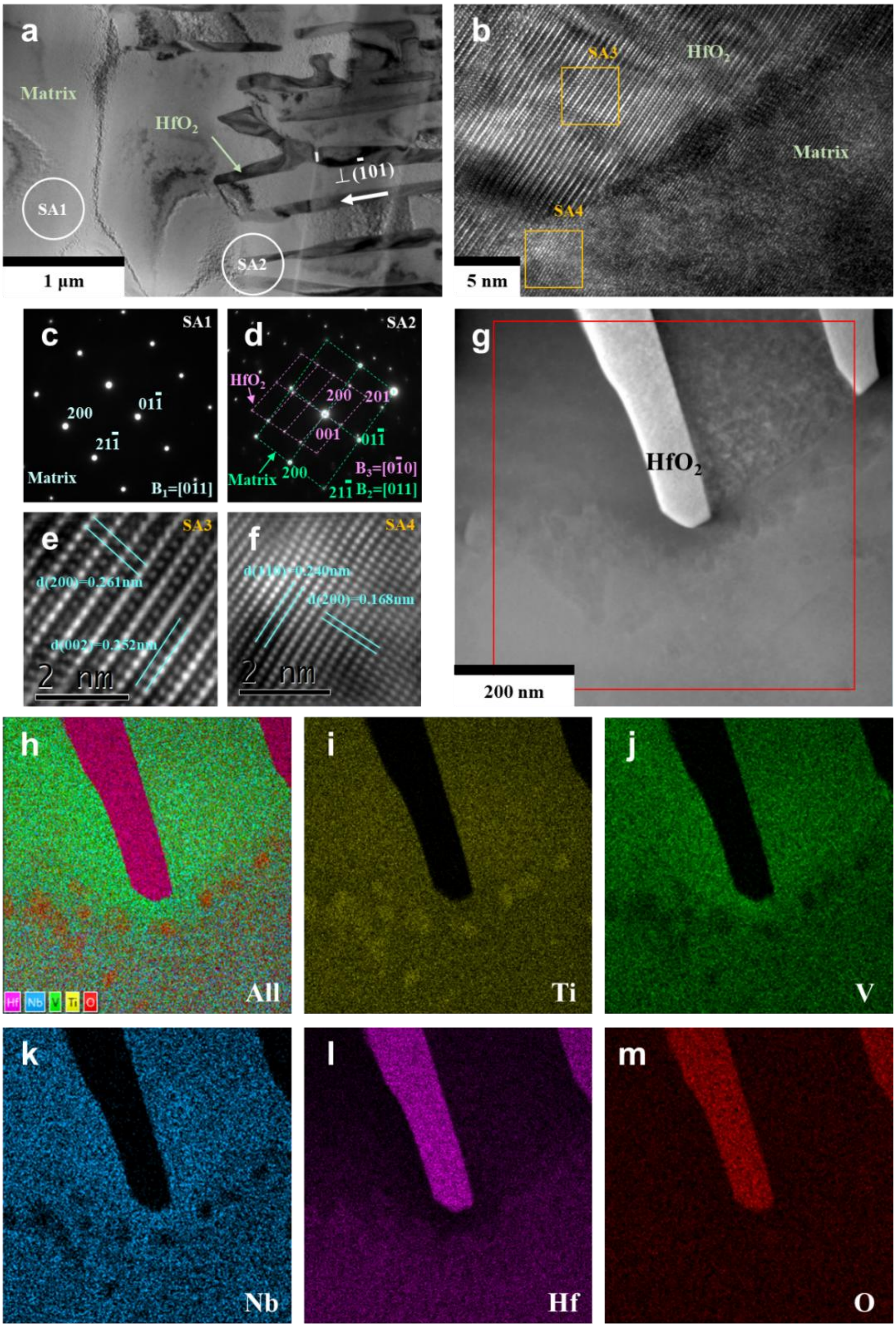

Fig. 9 TEM images of the front of needle-like HfO_2 under the condition of 1000°C-1min in air (the TEM sample was prepared by FIB as located in the position of FIB 3 in Fig. S2): (a) Bright-field TEM image; (b) High resolution bright-field (HRTEM) morphology

of the boundary of needle-like HfO_2 and matrix; (c-d) the corresponding SAED patterns of SA1 and SA2 in (a); (e-f) the corresponding Fast Fourier Transform (FFT) and inverse FFT of SA3 and SA4 in (b); (g) The STEM-HAADF image around the front of needle-like HfO_2; (h-m) The corresponding elemental distribution for the selected area of (g).

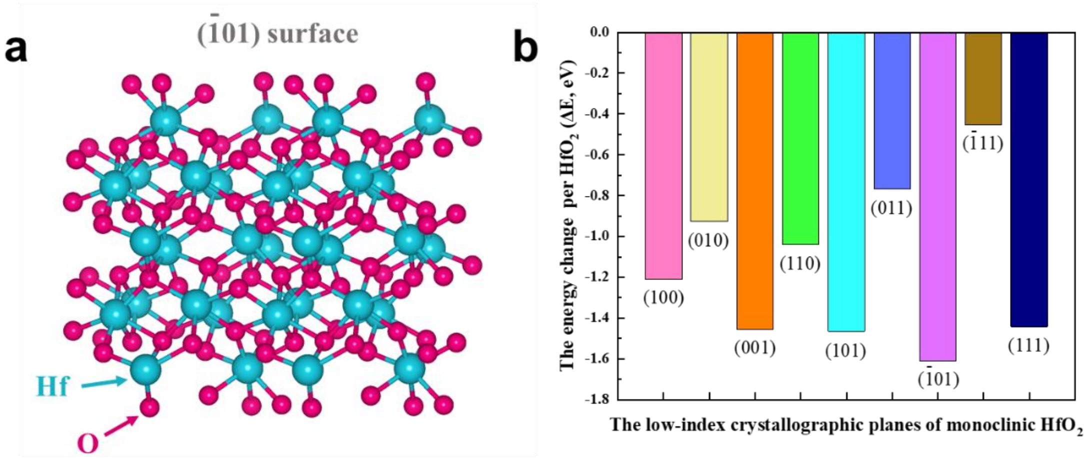

Fig. 10 (a) Atomic configuration of monoclinic HfO_2 calculated by DFT; (b) The calculated energy change when per HfO_2 grows along a certain crystallographic plane at 1000°C.

Based on the aforementioned discussion, the mechanisms for the oxidation of the RHEA alloy below and above 1000°C are schematically summarized in **Fig. 11**. When the temperature below 1000°C, a dense layer of composite oxide scale of $(Ti_{38}V_{15}Nb_{23}Hf_{24})O_x$ is formed on the surface of alloy matrix. The diffusivity of oxygen in the composite oxide scale is sluggish due to the highly consistent lattice constant and orientation among the oxide nanocrystallites. An external oxidation features occurs in such state. Further, when the temperature reaches up to 1000°C, the evaporation of V_2O_5 from the decomposed oxide scale causes the outward migration of Ti, Nb ions and the precipitation of HfO_2 particles in the oxide scale. Abundant interfaces are formed among oxide nanocrystallites, and sharply increase the diffusivity of oxygen in the oxide scale. The internal oxidation of needle-like HfO_2 growing in the alloy matrix is stimulated under the sufficient diffusivity of oxygen.

Based on the incoherent interfaces of the HfO_2/alloy matrix as well as the alloy matrix itself, the O continuously transfers to the growth front of the needles and combines with Hf in the alloy matrix. Therefore, the oxidation process is greatly accelerated by the internal oxidation and a weak oxidation resistance with fast oxidation kinetics is produced. The oxide scales in this alloy will continuously grow into the alloy matrix until the alloy is fully oxidized. That is because this alloy cannot form sufficiently dense passivation oxide layer (similar to Cr_2O_3, SiO_2, Al_2O_3) to completely prevent the diffusion of oxygen. In follow-up studies, we will devote to tailor the oxide scales to achieve an outstanding oxygen-shielded ability.

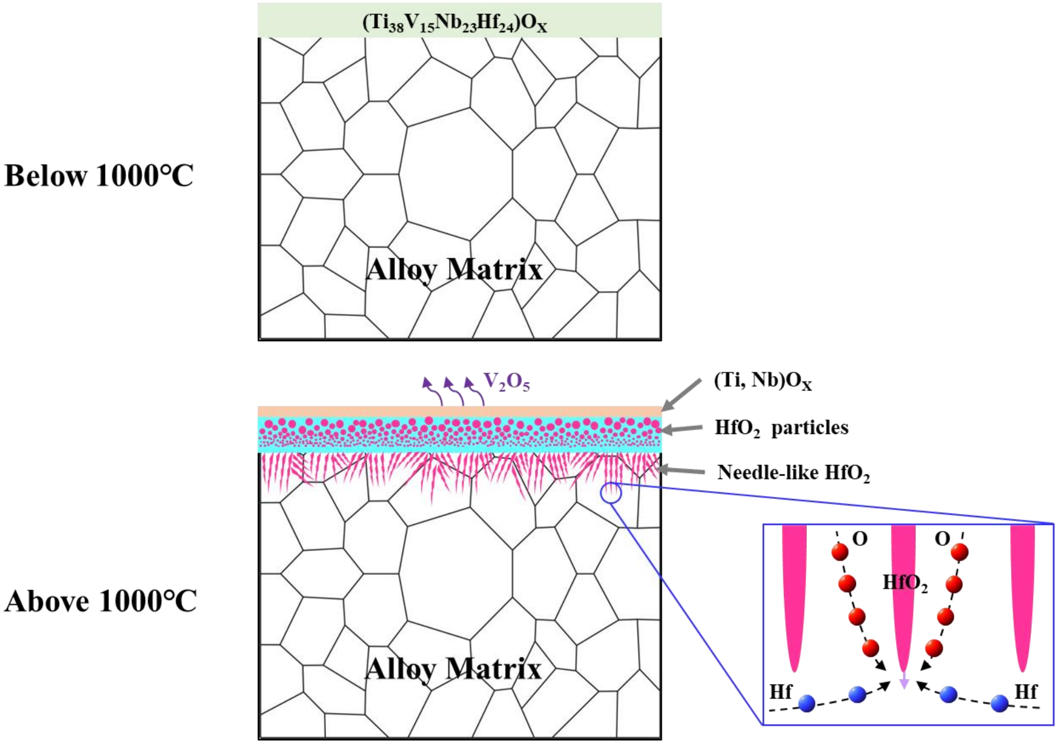

Fig. 11 Schematic of the oxidation mechanisms of the RHEA below and above 1000°C.

5. Conclusions

The oxidation behavior of the $Ti_{38}V_{15}Nb_{23}Hf_{24}$ refractory high-entropy alloy in air at various temperatures was systematically studied in this work. The conclusions are summarized as follows:

1) The dense composite oxide scale formed on the surface of RHEAs below 1000°C exhibits highly consistent lattice constant and crystallographic orientation, which is benefited in preventing the inward diffusion of oxygen and the outward diffusing of metallic ions.

2) The dense composite oxide is decomposed above 1000°C dues to the evaporation of V_2O_5, which promotes the formation of a sub-layer of oxide enriched Ti and Nb and the precipitation of HfO_2 with gradient distribution.

3) The decomposed composite oxide above 1000°C sharply increases the inward diffusivity of oxygen in the oxide scale. The inward-diffusing oxygen arriving at the alloy matrix reaches the critical value of internal oxidation, which causes the nucleation and growth of needle-like HfO_2 in the matrix with the preferred direction perpendicular to the $(\bar{1}01)$ plane.

4) The compositional gradient prompts Hf and O in distant regions in gathering to the front of needle-like HfO_2, and gradually exhausts the element of Hf in the alloy matrix.

Data availability

Experimental data from this study are available from Prof. Lin Liu from Huazhong University of Science and Technology upon reasonable request.

Acknowledgements

The work described in this paper was substantially supported by a grant from the NSFC/RGC Joint Research Scheme sponsored by the National Natural Science Foundation of China and the Research Grants Council of Hong Kong (Project No. 52061160483 and No. N_PolyU523/20), and National Postdoctoral Science Foundation of China (Project No. 2020M672336). Di Ouyang also acknowledge the financial support from the Postdoc Matching Fund Scheme of The Hong Kong Polytechnic University (Project No. P0035796/1-W17D). The authors are also grateful to the Analytical and Testing Center, Huazhong University of Science and Technology for technical assistance.

Author contributions

Di Ouyang prepared the samples, carried out the structural characterizations and wrote the draft; Zheng-jie Chen and Hai-bin Yu performed the DFT simulation; K. C. Chan supervised the RGC project and revised the manuscript; Lin Liu conceived and directed the project as well as revised the manuscript. All authors discussed the results and commented on the manuscript.

Competing interest

The authors declare no competing interests.

References

[1] E.P. George, D. Raabe, R.O. Ritchie, High-entropy alloys, Nat. Rev. Mater., 8 (2019) 515-534.

[2] Y. Zhang, T.T. Zuo, Z. Tang, M.C. Gao, K.A. Dahmen, P.K. Liaw, Z.P. Lu, Microstructures and properties of high-entropy alloys, Prog. Mater. Sci., 61 (2014) 1-93.

[3] Z. Li, S. Zhao, R.O. Ritchie, M.A. Meyers, Mechanical properties of high-entropy alloys with emphasis on face-centered cubic alloys, Prog. Mater. Sci., 102 (2019) 296-345.

[4] T. Li, Y. Lu, T. Wang, T. Li, Grouping strategy via d-orbit energy level to design eutectic high-entropy alloys, Appl. Phys. Lett., 119 (2021) 071905.

[5] O.N. Senkov, D.B. Miracle, K.J. Chaput, J.-P. Couzinie, Development and exploration of refractory high entropy alloys—A review, J. Mater. Res., 33 (2018) 3092-3128.

[6] D.B. Miracle, M.-H. Tsai, O.N. Senkov, V. Soni, R. Banerjee, Refractory high entropy superalloys, Scripta Mater., 187 (2020) 445-452.

[7] T. Li, Y. Lu, Z. Cao, T. Wang, T. Li, Opportunity and Challenge of Refractory High-Entropy Alloys in the Field of Reactor Structural Materials, Acta Metallurgica Sinica, 57 (2021) 42-54.

[8] A. Ayyagari, R. Salloom, S. Muskeri, S. Mukherjee, Low activation high entropy alloys for next generation nuclear applications, Materialia, 4 (2018) 99-103.

[9] O.N. Senkov, G.B. Wilks, D.B. Miracle, C.P. Chuang, P.K. Liaw, Refractory high-entropy alloys, Intermetallics, 18 (2010) 1758-1765.

[10] O.N. Senkov, G.B. Wilks, J.M. Scott, D.B. Miracle, Mechanical properties of Nb25Mo25Ta25W25 and V20Nb20Mo20Ta20W20 refractory high entropy alloys, Intermetallics, 19 (2011) 698-706.

[11] B. Vishwanadh, N. Sarkar, S. Gangil, S. Singh, R. Tewari, G.K. Dey, S. Banerjee, Synthesis and microstructural characterization of a novel multicomponent equiatomic ZrNbAlTiV high entropy alloy, Scripta Mater., 124 (2016) 146-150.

[12] T. Li, W. Jiao, J. Miao, Y. Lu, E. Guo, T. Wang, T. Li, P.K. Liaw, A novel ZrNbMoTaW refractory high-entropy alloy with in-situ forming heterogeneous structure, Mater. Sci. Eng. A, 827 (2021) 142061.

[13] B. Zhang, M.C. Gao, Y. Zhang, S. Yang, S.M. Guo, Senary refractory high entropy alloy MoNbTaTiVW, Mater. Sci. Technol., 31 (2015) 1207-1213.

[14] T. Li, J. Miao, Y. Lu, T. Wang, T. Li, Effect of Zr on the as-cast microstructure and mechanical properties of lightweight Ti2VNbMoZrx refractory high-entropy alloys, Int. J. Refract. Met. Hard Mater., 103 (2022) 105762.

[15] O.N. Senkov, J.M. Scott, S.V. Senkova, D.B. Miracle, C.F. Woodward, Microstructure and room temperature properties of a high-entropy TaNbHfZrTi alloy, J. Alloys Compd., 509

(2011) 6043-6048.

[16] O.N. Senkov, S.V. Senkova, D.B. Miracle, C. Woodward, Mechanical properties of low-density, refractory multi-principal element alloys of the Cr–Nb–Ti–V–Zr system, Mater. Sci. Eng. A, 565 (2013) 51-62.

[17] Z. Lei, X. Liu, Y. Wu, H. Wang, S. Jiang, S. Wang, X. Hui, Y. Wu, B. Gault, P. Kontis, D. Raabe, L. Gu, Q. Zhang, H. Chen, H. Wang, J. Liu, K. An, Q. Zeng, T.G. Nieh, Z. Lu, Enhanced strength and ductility in a high-entropy alloy via ordered oxygen complexes, Nature, 563 (2018) 546-550.

[18] S. Wei, S.J. Kim, J. Kang, Y. Zhang, Y. Zhang, T. Furuhara, E.S. Park, C.C. Tasan, Natural-mixing guided design of refractory high-entropy alloys with as-cast tensile ductility, Nat. Mater., 19 (2020) 1175-1181.

[19] B. Gorr, S. Schellert, F. Müller, H.-J. Christ, A. Kauffmann, M. Heilmaier, Current Status of Research on the Oxidation Behavior of Refractory High Entropy Alloys, Adv. Eng. Mater., 23 (2021) 20011047.

[20] C.M. Liu, H.M. Wang, S.Q. Zhang, H.B. Tang, A.L. Zhang, Microstructure and oxidation behavior of new refractory high entropy alloys, J. Alloys Compd., 583 (2014) 162-169.

[21] B. Gorr, M. Azim, H.J. Christ, T. Mueller, D. Schliephake, M. Heilmaier, Phase equilibria, microstructure, and high temperature oxidation resistance of novel refractory high-entropy alloys, J. Alloys Compd., 624 (2015) 270-278.

[22] T.M. Butler, K.J. Chaput, J.R. Dietrich, O.N. Senkov, High temperature oxidation behaviors of equimolar NbTiZrV and NbTiZrCr refractory complex concentrated alloys (RCCAs), J. Alloys Compd., 729 (2017) 1004-1019.

[23] F. Müller, B. Gorr, H.-J. Christ, J. Müller, B. Butz, H. Chen, A. Kauffmann, M. Heilmaier, On the oxidation mechanism of refractory high entropy alloys, Corros. Sci., 159 (2019) 108161.

[24] S. Sheikh, M.K. Bijaksana, A. Motallebzadeh, S. Shafeie, A. Lozinko, L. Gan, T.-K. Tsao, U. Klement, D. Canadinc, H. Murakami, S. Guo, Accelerated oxidation in ductile refractory high-entropy alloys, Intermetallics, 97 (2018) 58-66.

[25] N. Birks, G.H. Meier, F.S. Pettit, Introduction to the High-Temperature Oxidation of Metals, Cambridge University Press, 2006.

[26] M. Pole, M. Sadeghilaridjani, J. Shittu, A. Ayyagari, S. Mukherjee, High temperature wear behavior of refractory high entropy alloys based on 4-5-6 elemental palette, J. Alloys Compd., 843 (2020) 156004.

[27] D.J. Young, High temperature oxidation and corrosion of metals, Elsevier, 2008.

[28] A.B. Mukhopadhyay, J.F. Sanz, C.B. Musgrave, First-principles calculations of structural and electronic properties of monoclinic hafnia surfaces, Phys. Rev. B, 73 (2006).

[29] D.L. Douglass, A Critique of Internal Oxidation in Alloys During the Post-Wagner Era, Oxid. Met., 44 (1995) 81-111.

[30] D.B. Williams, C.B. Carter, Transmission Electron Microscopy A Textbook for Materials Science, 2 ed., Springer, Boston, MA, 2009.

[31] E.M. Savitskii, G.S. Burkhanov, Physical Metallurgy of Refractory Metals and Alloys, Springer Science & Business Media, 1970.

[32] www.factsage.com.

[33] P.Massard, J.C.Bernier, A.Michel, Effet Jahn-Teller dans le système Ta2CrO6-TaCrO4, J.

Solid State Chem., 4 (1972) 269-274.

[34] J.G. Keller, D.L. Douglass, The High-Temperature Oxidation Behavior of Vanadium-Aluminum Alloys Oxid. Met., 36 (1991) 439-464.

[35] N. Yurchenko, E. Panina, S. Zherebtsov, G. Salishchev, N. Stepanov, Oxidation Behavior of Refractory AlNbTiVZr0.25 High-Entropy Alloy, Materials, 11 (2018).

[36] B. Gorr, F. Mueller, H.J. Christ, T. Mueller, H. Chen, A. Kauffmann, M. Heilmaier, High temperature oxidation behavior of an equimolar refractory metal-based alloy 20Nb 20Mo 20Cr 20Ti 20Al with and without Si addition, J. Alloys Compd., 688 (2016) 468-477.

[37] S. Sheikh, L. Gan, A. Ikeda, H. Murakami, S. Guo, Alloying effect on the oxidation behavior of a ductile Al0.5Cr0.25Nb0.5Ta0.5Ti1.5 refractory high-entropy alloy, Materials Today Advances, 7 (2020) 100104.

[38] P.J. Nolan, P.J. Grundy, The Morphology and Stability of Precipitates in Internally Oxidised Silicon-bearing Nickel and Cobalt Alloys, J. Mater. Sci., 6 (1971) 1143-1150.

[39] R.A. Rapp, Kinetics, Microstructures and Mechanism of Internal Oxidation - Its Effect and Prevention in High Temperature Alloy Oxidation, Corrosion, 21 (1965) 382-401.

[40] B. Aguirre, R.S. Vemuri, D. Zubia, M.H. Engelhard, V. Shutthananadan, K.K. Bharathi, C.V. Ramana, Growth, microstructure and electrical properties of sputter-deposited hafnium oxide (HfO2) thin films grown using a HfO2 ceramic target, Appl. Surf. Sci., 257 (2011) 2197-2202.